MDPI

*Article*

# Numerical Simulation of Turbulent Flow in Bends and Confluences Considering Free Surface Changes Using the Volume of Fluid Method

Rawaa Shaheed [1,*], Abdolmajid Mohammadian [1] and Xiaohui Yan [2]

1    Department of Civil Engineering, University of Ottawa, 75 Laurier Ave E, Ottawa, ON K1N 6N5, Canada; majid.mohammadian@uottawa.ca
2    School of Water Resources Engineering, Dalian University of Technology, 2 Ling Gong Road, Dalian 116024, China; yanxh@dlut.edu.cn
*    Correspondence: rshah015@uottawa.ca

**Abstract:** The impact of secondary flows on the flow velocity in open channel bends and confluences was simulated using three-dimensional (3D) numerical models. The Reynolds-averaged Navier–Stokes equation system was utilized as the governing equations and two different turbulence models were employed in this study: the standard k-$\varepsilon$ model and the realizable k–$\varepsilon$ model. In a recent study by the authors, the rigid lid approach was used, which does not allow for vertical displacement of the water surface. In this study, the simulation of free surface displacements was simulated using the volume of fluid free-surface tracking method. The numerical models were evaluated and validated by using the experimental data of a sharply curved channel and a confluent channel. The accuracies of the two turbulence models were evaluated and discussed. This study found that both models can satisfactorily reproduce the experimental data. However, the standard k–$\varepsilon$ model performed better for the curved channel case while the Realizable k–$\varepsilon$ model performed better for the confluent channel case.

**Keywords:** secondary flow; free surface model; standard k–$\varepsilon$; realizable k–$\varepsilon$; OpenFOAM

## 1. Introduction

The flow pattern in curved rivers and confluences is fairly complex due to the high turbulence and the three-dimensional (3D) flow characteristics. The flow in such areas is affected by the centrifugal force that results in a lateral gradient on the water's surface, which leads to a lateral pressure gradient at the cross-section [1]. The interaction between the centrifugal force and the lateral pressure gradients due to the lateral slope of the water's surface results in the generation of secondary flow in the transverse direction of the bend [2]. The helical motion of the secondary flow causes the particles near the bed to move inwards, and those near the water's surface to move outwards (Figure 1). Considering the impact of the secondary flow and velocity distribution on the flow pattern of open channel curves is of high significance due to its effect on erosion and sedimentation patterns in rivers [3], and transport of the pollutants.

The flow in curved rivers and confluences have been significantly studied in recent decades. Due to the merits of low-cost and high-efficiency, numerical modeling techniques have been widely adopted. The flow in curved rivers has been studied numerically by numerous studies using different kinds of numerical models due to the intricacy of flow features in this field. Some of these studies are described below.

The flow in rotating annular flumes at a mildly-curved 180° bend and a mildly curved river was measured and simulated by Booij [4] through the use of Large Eddy Simulation (LES) and Reynolds-Averaged Navier-Stokes (RANS) (standard k-$\varepsilon$) models. He concluded that the main features of the main flow and the secondary flow can be produced by the

RANS model, but it failed to satisfactorily reproduce the complicated secondary flow fields in both curved flows. The pattern of the secondary flow computed by LES hardly deviated from the measured flow pattern in the rotative annular flume, and the turbulence was reproduced correctly. The main and secondary flow fields were reproduced well by LES for the slightly curved river. The second, counter-rotating, secondary flow cell along the upper external riverbank was yielded by LES computations, which contrasts with RANS computations.
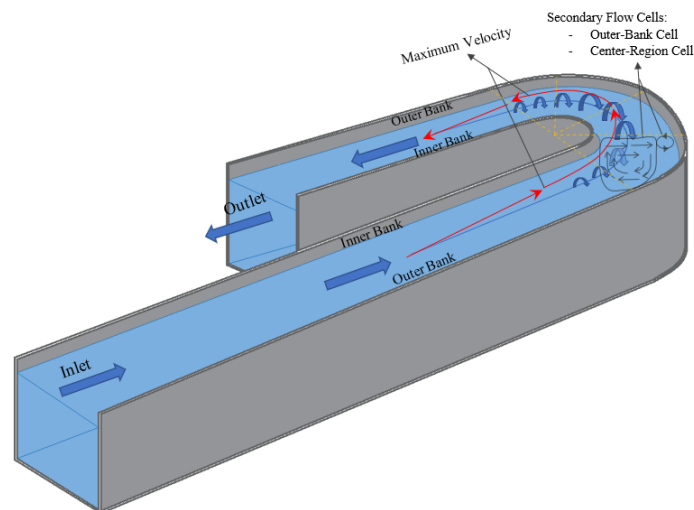


**Figure 1.** Flow pattern in a curved channel.

The secondary flows in a spacious curved channel were studied by Huang et al. [5] using a 3-D free-surface turbulence model with two turbulence closure schemes using two pressure solution methods. The turbulence closure schemes included a mixing-length model and the standard k-ε model, and the pressure solution methods included hydrostatic presumptions and dynamic pressure treatments. A similar pattern of secondary flow was produced by the mixing length model with static and dynamic pressure treatments, and the center-region cell of the secondary flow could be predicted as well. In addition, a similar pattern of secondary flow was generated by the standard k-ε model with either static or dynamic pressure treatments, and the presence of the outer-bank cell and the center-region cell of secondary flows could also be predicted.

Detached Eddy Simulation (DES) was used by Constantinescu et al. [6] to calculate the turbulence structure and the flow in an open channel 193° bend of very high curvature. The experimental data of Blanckaert [7] was used to apply the model and compare the three-dimensional velocity distributions predicted by DES. The predicted results by DES to capture the distribution of the streamwise velocity in the mean flow, and the streamwise vorticity distribution in relevant cross-sections were satisfactory. Furthermore, the simulations indicated that DES is considerably more successful than Reynolds Averaged Navier Stokes (RANS) in forecasting the velocity redistribution in the channel.

The experimental data of Blanckaert [7] was used by van Balen et al. [8] to detect the characteristics of the main and secondary flow by applying and comparing large-eddy simulations (LES) and Reynolds-averaged numerical simulations (RANS) in a curved open channel. The strength of secondary flow depends significantly on the turbulence in river bends which in turn plays a significant role in the substantial processes in natural rivers and especially in the flow areas close to the banks. The intensity of the center region cell was under anticipated by the RANS model and well anticipated by the LES model. The outer-bank cell of secondary flow was resolved accurately by LES, while RANS was unable to reproduce this process. The bed shear stress was overestimated by RANS as compared with LES. Consequently, overall friction losses that were measured experimentally over the bend were reproduced properly by LES, while they were overestimated by RANS.

The pattern of the flow in a 90° bend was studied empirically and numerically by Abhari et al. [9] using the Sediment Simulation In Intakes with Multiblock (SSIIM 1.1) numerical model. The turbulence was expected by k-ε model, and the pressure was computed by the Semi-Implicit Method for Pressure Linked Equations (SIMPLE) method. A comparison of the results between the numerical model and the experimental data indicated the capability of SSIIM-1.1 in simulating the flow pattern accurately.

The flow patterns in a highly bent 90° open channel curve were studied experimentally and numerically by Gholami et al. [10]. The water-free surface was simulated using the volume of fluid (VOF) method and the turbulence was predicted by the k-ε (RNG) model. The results indicated that the higher flow velocity occurred close to the interior wall along the bend, and the influence of the secondary flows was not limited to the sections within the bend. Additionally, the k-ε (RNG) model and VOF methods have the capability to simulate the flow pattern in the strongly curved bends.

The experimental data of Blanckaert [7] was also used by Abdou et al. [11] to study the flow features in a strongly-curved open channel using the LES turbulence model. They concluded that the LES model had the capability to predict the produced super-elevation, stream and transverse velocities, and the two secondary circulation cells (main and outer bank cells).

The free surface flow in a steeply curved open channel with a 30° bend was studied numerically by Seyedashraf and Akhtari [12]. The experimental data of a sharp 90° bend was used to authorize the simulation results of the numerical model in a sharp 30° bend. The standard k-ε turbulence model and volume of fluid free-surface tracking method were used for the air-water interactions and turbulence closure. The results showed that the intensity of secondary flow in a 30° bend is minor compared to the 90° bend. However, in these curves, the tendency toward flow separation is more intense because of the momentum of the liquid molecules passing the bend.

The experimental data of Rozovskii [13] that includes a 180° sharply curved channel was used by Shaheed et al. [14] to evaluate the rigid lid model in the simulation of flow in curved channels. Two turbulence models (standard k–ε and realizable k–ε) were applied in this study. The results showed that both two models simulated the flow in the curved channel well. However, the standard k–ε model performed better than the realizable k–ε model.

The other common phenomenon in natural rivers is open-channel confluences that play an important role in hydraulic engineering works due to the complex interaction between the main channel and tributary flows. This complex interaction generates complex turbulent structures and leads to the evolution of six distinct zones [15] (Figure 2): stagnation zone, deflection zone, separation zone, shear layers zone, extreme velocity zone, and recovery zone. Several variables could affect these turbulent structures like the discharge of the two channels, the junction angle, and the geometry of the channel. Thus, studying the features of this flow in such areas is not an easy matter and requires an important tool such as numerical simulation [16]. In channel confluences, there are two counter-rotating helical cells: the secondary flow of the branch channel near the inner bank downstream of the main channel, and the secondary flow of the main channel near the outer bank downstream of the major channel (Figure 2). Because of the fluid viscosity, the two secondary flows fade gradually downstream of the main channel [17].

The complex flow characteristics in confluent channels have been studied numerically by many researchers using different kinds of numerical models. Some of these studies are described below.
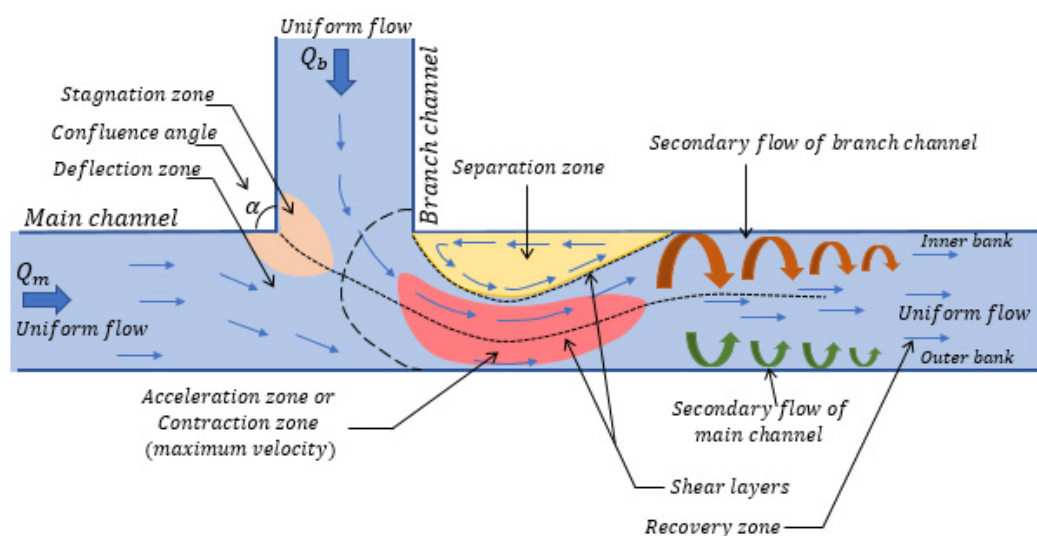
**Figure 2.** Flow pattern in a confluent channel (based on [18], from [15]), and secondary flow structure in a confluent channel (based on [17] after [19], (developed from [20]).

The flow in a 90° open channel junction was studied by Huang et al. [21] using a three-dimensional numerical model. Reynolds-averaged Navier–Stokes (RANS) equations with incompressible and steady-state assumptions were employed, and the k–ω model of Wilcox [22] was selected for this study. The experimental data of Shumate [23] was used to validate the model with two distinctive flow discharges. Then, the influence of varying junction angles on flow characteristics was studied by applying this model. Consequently, they found that the significant hydrodynamic features of the flow in the junction were all reproduced by the developed 3D model, with a favorable agreement with the experimental data.

The flow structure in channel confluences was studied by Shakibaeinia et al. [18] using a three-dimensional numerical model (SSIIM2.0) developed by Olsen [24] and based on a finite volume discretization of Reynolds averaged Navier Stokes equations. The Re-Normalization Group RNG form of the k-ε turbulence model was practiced. The numerical model was first validated by comparing the simulated results with the experimental data of Shumate and Weber [25], and then it was applied to examine secondary flows, velocity distribution, flow separation, and elevation of water surface under various circumstances. The results showed that a strong tributary helical cell occurred in the post confluence channel due to the flow deflection. There was also a weaker helical cell created by the main flow, which rotates against the tributary helical cell. The results also showed that the confluence angle, discharge, width ratio, and Froude number significantly affected the flow structure and water surface variation because of their impact on flow deflection, secondary flows, and separation zone.

The experimental data of Weber et al. [19] was used by Yang et al. [26] to simulate the flow numerically in a right angle confluence open channel with the dynamic mesh technique. ANSYS FLUENT and three numerical models including standard k-ε, realizable k-ε, and k-ω were used to conduct the simulation. The surface position was tracked using three types of surface treatment methods: rigid lid, volume of fluid (VOF), and self-proposed codes with dynamic mesh technique. The results showed that the accuracy of the simulation was impacted greatly by the method of surface treatment for the same adopted turbulence models. The free surface was treated as an assumed surface in the method of the rigid lid, and a large error was generated when the actual surface differed greatly. The precision of the VOF method was better than the rigid lid process as it captured the free surface via a multi-phase model. However, for the shallow water flow, the accuracy was still poor. The dynamic mesh technique showed a good agreement with the experimental

data, and turbulence models showed little effect on water level tracking. The k-ω model was preferable for the distribution of velocity in the confluence flow simulation.

The flow at a 70° open-channel confluence was studied by Brito et al. [16] using a 3D numerical simulation. The simulation was conducted using Reynolds-averaged Navier-Stokes (RANS) equations and five turbulence closure models including: k-ε, RNG k-ε, k-ω, SST k-ω, and Explicit Algebraic Reynolds Stress Models (EARSM). The interaction between the air and water at the free surface was modeled by the volume of fluid (VoF) method as well. The results of the simulation were compared with the experimental data of Birjukova et al. [27], which demonstrated that simple two-equation turbulence models are insufficient to obtain an accurate flow field description in confluences due to the complexity of flows at such areas. The EARSM showed a reasonably good representation for the separation zone while it underestimated the time-averaged streamwise velocity in the maximum velocity zone.

The experimental data of Shumate [23] that includes a 90° angle confluent channel was used by Shaheed et al. [14] to evaluate the rigid lid model in the simulation of flow in confluent channels. Two turbulence models (standard k–ε and realizable k–ε) were applied in this study. The results showed that both two models simulated the flow in the confluent channel well. However, the realizable k–ε model performed better than the standard k–ε model.

However, there is a gap in the literature about the performance of different turbulence models in predicting the secondary flow in channel bends and confluences while simulating free surface displacements. In [14] a rigid lid approach was used prohibited vertical motions of the free surface. This study employed two turbulence models to simulate the dynamics of free surface displacement, the volume of fluid methods is used. Therefore, the primary aim of this study is to comprehend what range of selected turbulence models can model the flow field in open channel curves and confluences. In view of this, two commonly used effective turbulence models (standard k–ε and realizable k–ε) were selected to evaluate their performance in such simulations.

## 2. Numerical Modeling

Numerical modeling has recently become one of the widely used methods in studying river flows, and in this study, the OpenFOAM (Open Field Operation and Manipulation) model was utilized in this study to simulate the flow in curved rivers and confluences. OpenFOAM uses the finite volume method and contains different numerical schemes that are employed for both time and space integration. More information about OpenFOAM has been well documented in the user manual [28]. InterFoam solver is used in this study, which is usually utilized for incompressible and turbulent flows in the cases of open channels (also referred to as the Free Surface Model). The free water surface was simulated using the volume of fluid (VOF) method and the turbulence was predicted using standard k–ε and realizable k–ε turbulence models. The basic concept of the VOF technique is to define functions to represent the volume fraction (relative proportion of volume) of water and air in the model area. In each cell, the sum of the volume fractions of water and air is 1. For a computing cell, there are three situations:

$\alpha = 1$ means that the cell is filled with water, $\alpha = 0$ means that the cell is filled with air, and $0 < \alpha < 1$ means that the cell has a water-air interface.

The 3D Reynolds–Averaged Navier–Stokes equations (RANS) for mass and momentum conservation can be expressed as follows:

Continuity:

$$\frac{\partial}{\partial x}(u_x) + \frac{\partial}{\partial y}(u_y) + \frac{\partial}{\partial z}(u_z) = 0 \tag{1}$$

Momentum in the *x*-direction:

$$\frac{\partial(\rho u_x)}{\partial t} + \frac{\partial}{\partial x}(\rho u_x u_x) + \frac{\partial}{\partial y}(\rho u_y u_x) + \frac{\partial}{\partial z}(\rho u_z u_x) = -\frac{\partial p}{\partial x} + \frac{\partial \tau_{xx}}{\partial x} + \frac{\partial \tau_{yx}}{\partial y} + \frac{\partial \tau_{zx}}{\partial z} + \rho g_x \tag{2}$$

Momentum in the *y*-direction:

$$\frac{\partial(\rho u_y)}{\partial t} + \frac{\partial}{\partial x}(\rho u_x u_y) + \frac{\partial}{\partial y}(\rho u_y u_y) + \frac{\partial}{\partial z}(\rho u_z u_y) = -\frac{\partial p}{\partial y} + \frac{\partial \tau_{xy}}{\partial x} + \frac{\partial \tau_{yy}}{\partial y} + \frac{\partial \tau_{zy}}{\partial z} + \rho g_y \quad (3)$$

Momentum in the *z*-direction:

$$\frac{\partial(\rho u_z)}{\partial t} + \frac{\partial}{\partial x}(\rho u_x u_z) + \frac{\partial}{\partial y}(\rho u_y u_z) + \frac{\partial}{\partial z}(\rho u_z u_z) = -\frac{\partial p}{\partial z} + \frac{\partial \tau_{xz}}{\partial x} + \frac{\partial \tau_{yz}}{\partial y} + \frac{\partial \tau_{zz}}{\partial z} + \rho g_z \quad (4)$$

where $\rho$ is the density; $t$ is the time, $u_x$, $u_y$, and $u_z$ are the velocity components in the $x$, $y$, and $z$ directions respectively; $p$ is the pressure; $\tau_{ij}$ denotes a stress in the $j$-direction exerted on a plane perpendicular to the $i$-axis; $g_x$, $g_y$, and $g_z$ are the gravitational acceleration components in the $x$, $y$, and $z$ directions respectively [29].

The OpenFOAM numerical model solves the Navier Stokes equations with the two models on a three-dimensional grid. The continuity equation and the Reynolds averaged Navier-Stokes equations are solved to determine the flow field for three-dimensional geometry. The turbulence model's objective is to close the RANS equations and to compute the Reynolds stresses. Standard k–ε [30]) and realizable k–ε [31] turbulence models are two-equation models. Two extra transport equations are included in these models to represent the turbulent flow properties. The first transport variable is turbulent kinetic energy, k, and the second is the turbulent dissipation, ε.

The standard k–ε model can be written as:

$$\frac{\partial k}{\partial t} + \frac{\partial k u_i}{\partial x_i} - \frac{\partial}{\partial x_i}\left(D_{keff}\frac{\partial k}{\partial x_i}\right) = G - \varepsilon \quad (5)$$

$$\frac{\partial \varepsilon}{\partial t} + \frac{\partial \varepsilon u_i}{\partial x_i} - \frac{\partial}{\partial x_i}\left(D_{\varepsilon eff}\frac{\partial \varepsilon}{\partial x_i}\right) = c_{1\varepsilon}\frac{\varepsilon}{k}G - c_{2\varepsilon}\frac{\varepsilon^2}{k} \quad (6)$$

$$D_{keff} = \nu_t + \nu \quad (7)$$

$$D_{\varepsilon eff} = \frac{\nu_t}{\sigma_\varepsilon} + \nu \quad (8)$$

$$\nu_t = c_\mu \frac{k^2}{\varepsilon} \quad (9)$$

$$G = 2\nu_t S_{ij} S_{ij} \quad (10)$$

$$S_{ij} = \frac{1}{2}\left(\frac{\partial u_j}{\partial x_i} + \frac{\partial u_i}{\partial x_j}\right) \quad (11)$$

where $\sigma_\varepsilon$, $c_{1\varepsilon}$, $c_{2\varepsilon}$, $c_\mu$ are model constants equal to 1.3, 1.44, 1.92, and 0.09, respectively; $k$ is the turbulent kinetic energy; $\varepsilon$ is the turbulent energy dissipation rate; $u_i$ is the instantaneous velocity component in the direction $x_i$; $D_{keff}$ and $D_{\varepsilon eff}$ are the effective diffusivity for $k$ and $\varepsilon$, respectively; $\nu_t$ is the turbulent kinematic viscosity; $\nu$ is the kinematic viscosity; $G$ is the production of turbulence due to shear; $S_{ij}$ is the strain-rate tensor; *dev* denotes the deviatoric component.

The Realizable *k–ε* model employed in the present study can be expressed as:

$$\frac{\partial k}{\partial t} + \frac{\partial k u_i}{\partial x_i} - \frac{\partial}{\partial x_i}\left(D_{keff}\frac{\partial k}{\partial x_i}\right) = G - \varepsilon \quad (12)$$

$$\frac{\partial \varepsilon}{\partial t} + \frac{\partial \varepsilon u_i}{\partial x_i} - \frac{\partial}{\partial x_i}\left(D_{\varepsilon eff}\frac{\partial \varepsilon}{\partial x_i}\right) = \sqrt{2}c_{1\varepsilon}S_{ij}\varepsilon - c_{2\varepsilon}\frac{\varepsilon^2}{k + \sqrt{\nu\varepsilon}} \quad (13)$$

$$D_{keff} = \frac{\nu_t}{\sigma_k} + \nu \quad (14)$$

$$D_{\varepsilon eff} = \frac{\nu_t}{\sigma_\varepsilon} + \nu \tag{15}$$

$$\nu_t = C_{\mu r}\frac{k^2}{\varepsilon} \tag{16}$$

$$C_{\mu r} = \frac{1}{A_0 + A_s U_s \frac{k}{\varepsilon}} \tag{17}$$

$$A_s = \sqrt{6}\cos\varphi_s \tag{18}$$

$$\varphi_s = \frac{1}{3}arccos\left\{\min\left[\max\left(\sqrt{6}W, -1\right), 1\right]\right\} \tag{19}$$

$$W = \frac{2\sqrt{2}S_{ij}S_{jk}S_{ki}}{S_{mag}S_2} \tag{20}$$

$$S_{mag} = \sqrt{S_2} \tag{21}$$

$$S_2 = 2\left(dev\left(S_{ij}\right)\right)^2 \tag{22}$$

$$S_{ij} = \frac{1}{2}\left(\frac{\partial u_j}{\partial x_i} + \frac{\partial u_i}{\partial x_j}\right) \tag{23}$$

$$U_s = \sqrt{\frac{S_2}{2} + \Omega_{ij}\Omega_{ij}} \tag{24}$$

$$\Omega_{ij} = \frac{1}{2}\left(\frac{\partial u_j}{\partial x_i} - \frac{\partial u_i}{\partial x_j}\right) \tag{25}$$

$$G = \nu_t S_2 \tag{26}$$

$$c_{1\varepsilon} = \max\left(\frac{\eta}{5+\eta}, 0.43\right) \tag{27}$$

$$\eta = S_{mag}\frac{k}{\varepsilon} \tag{28}$$

where $\Omega_{ij}$ is the vorticity (spin) tensor; $\sigma_k$, $\sigma_\varepsilon$, $A_0$, $c_{2\varepsilon}$ are model constants equal to 1, 1.2, 4, and 1.9 respectively.

The boundary of the flow inlet was set as a velocity inlet condition which was (0.265 m/s) for the curved channel and (0.628) for the confluent channel, and the flow outlet was set as a zero-gradient boundary condition. The boundary of the free surface was set as an atmospheric boundary condition. The standard wall functions [32] were used for the sidewalls and bed. The free surface was modeled using the volume of method (VOF) according to the following equation:

$$\frac{\partial \alpha}{\partial t} + \frac{\partial(\alpha x)}{x} + \frac{\partial(\alpha y)}{y} + \frac{\partial(\alpha z)}{z} = 0 \tag{29}$$

## 3. Verification of Numerical Model

### 3.1. Curved Channel

One of the previous experimental studies on curved channels is the experimental study of Rozovskii [13] who reported the results of velocity fields and water surface in a 180-degree sharp curved channel. The numerical model was utilized to simulate the experiment of Rozovskii, the channel setup of which is demonstrated in Figure 3. This channel consisted of a straight channel in a 6 m length followed by a 180° curve with a mean radius of 0.8 m and then the outlet in a 3 m straight channel length. The cross-section was a 0.8 m wide rectangle, and the whole channel was set on a horizontal bed [17]. The channel's characteristics and some hydraulic data gained from Rozovskii's experiment are shown in Table 1.
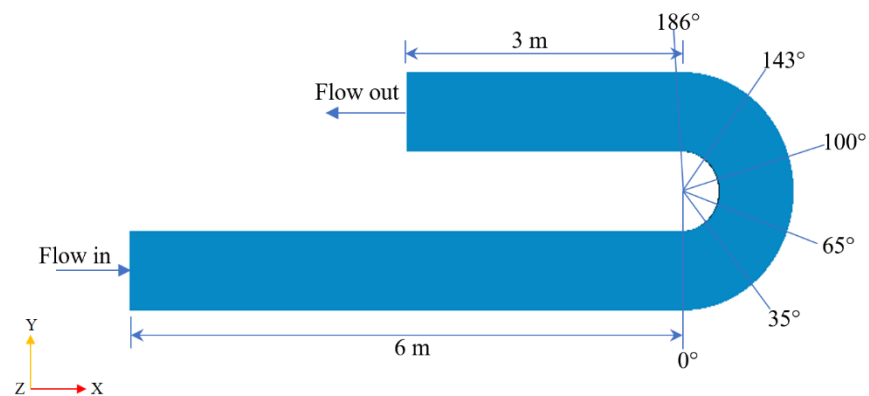
**Figure 3.** Rozovskii's experimental data [14].

**Table 1.** The flow conditions and dimensions of the curved channel [13].

| Variable | Symbol | Value |
|---|---|---|
| Upstream discharge | $Q$ | 0.0123 m³/s |
| Downstream water depth | $h$ | 0.058 m |
| Channel width | $B$ | 0.8 m |
| Bend angle | $\theta$ | 180° |
| Internal radius of curvature | $r_i$ | 0.4 m |
| Mean radius of curvature | $r_c$ | 0.8 m |
| Mean radius to width rati | $r_c/B$ | 1.0 |
| Che'zy factor | $C$ | 60 |
| Mean velocity at downstream | $U_\infty$ | 0.265 m/s |
| Tailwater Froude number | $Fr_d$ | 0.35 |

### 3.1.1. Boundary Conditions and Mesh Generation

The model of the curved channel includes four different boundaries as shown in Figure 4: the inlet, the outlet, the walls (side-walls and bottom), and the channel surface (atmosphere). The mesh that was used in the simulation is shown in Figure 5 and it was refined to better resolve the velocity, especially at the curve which is the study area and near the two banks of the channel. The mesh resolution was determined based on mesh sensitivity analyses: the results obtained by the current mesh and those provided by a finer mesh were almost identical. The flow was discharged with a primary velocity of $U_0$. The boundary conditions were chosen as: $u_x = U_0$; $u_y = u_z = 0$; $k = 0.06u^2$; and $\varepsilon = 0.06u^3 D$, where $D$ is the average water depth. The Courant number in all cases was kept below 0.9.
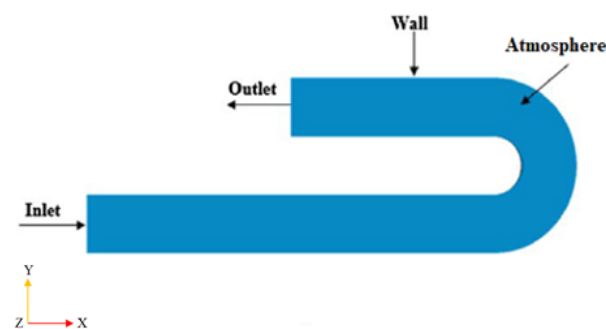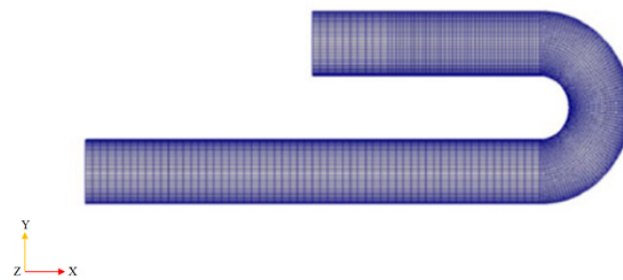


**Figure 4.** Boundary conditions.

**Figure 5.** The refined mesh.

*3.2. Results of Curved Channel*

3.2.1. Velocity Distribution

The velocity distribution of the curved open channel is shown in Figures 6 and 7 for the two numerical models. It appeared that the maximum velocity moved from the internal bank at the start of the curve to the external bank near the exit of the bend, which is consistent with previous experimental and numerical studies for bend flow [14,33].



**Figure 6.** The distribution of water surface velocity (Standard k-$\varepsilon$).



**Figure 7.** The distribution of water surface velocity (Realizable k-$\varepsilon$).

3.2.2. Longitudinal Velocity Distribution

The simulated longitudinal velocity of the curved open channel for the two numerical models was compared with the experimental data of Vaghefi et al. [1], who performed their experiment in a 180° curved open channel with some difference in dimensions from the experiment of Rozovskii [13]. The simulated longitudinal velocity at the section close to the water surface agreed well with the experimental data, as shown in Figure 8.

3.2.3. Properties of Flow Velocity

Figure 9 shows the depth-averaged velocity across the width of the channel, where: $U$ is the depth averaged velocity magnitude; and $u$, $v$, and $w$ are the longitudinal, vertical, and lateral velocity averaged over depth, respectively. Note that the depth-averaged velocity is represented by the vertical axis and is non-dimensionalized by $U_1$, which is the downstream mean velocity. The horizontal axis represents the radial distance $(r - r_i)/B$, non-dimensionalized by the channel width; where $B$ is the channel width and $r$ and $r_i$ are

the radius of curvature for the outer and inner banks, respectively. The velocity of the flow at the bend area was examined by taking some cross-sections at different locations of the bend including (0°, 35°, 65°, 100°, 143°, and 186°), as shown in the figure. The two numerical models were compared with the experimental data [13] and other models of other researchers [14,34–36] in these sections as well. It is clear from these cross-sections that the velocity of the flow increased near the interior bank at the beginning of the bend and then moved towards the exterior bank near the exit of the bend. Both numerical models performed well with some minor differences, especially near the two-channel banks. The flow near the banks is subjected to the effects of anisotropy, so it is quite common that a numerical model performed relatively worse in these regions.
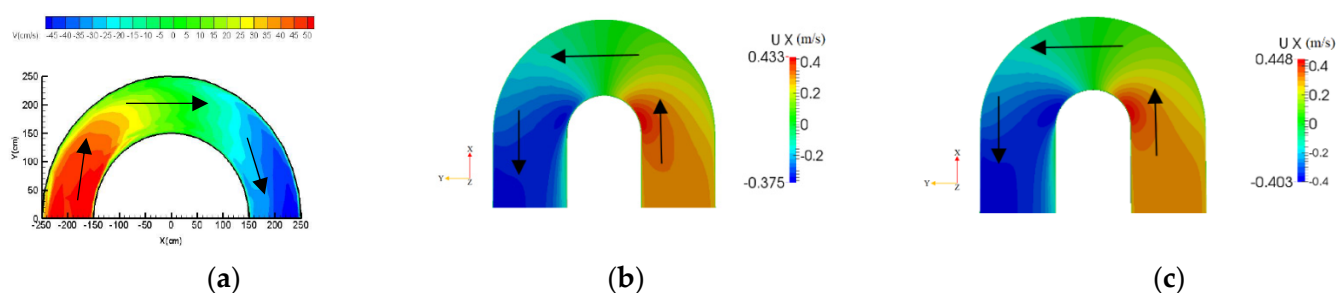


**Figure 8.** Longitudinal velocity contours. (**a**) contours of longitudinal velocity in the plan views—experiment (Vaghefi et al., 2015) [1]; (**b**) contours of longitudinal velocity in the plan views—simulated (Standard k-ε); (**c**) contours of longitudinal velocity in the plan views—simulated (Realizable k-ε).

To further assess the performance of the numerical models, the index root-mean-squared error (RMSE) was used to quantify the agreement between the two models and the experiment.

$$\text{RMSE} = \sqrt{\sum_{i=1}^{n} \frac{(\hat{y}_i - y_i)^2}{n}} \tag{30}$$

where $n$ is the number of observations, and $\hat{y}_i$ are predicted values, $y_i$ is observed values.

Table 2 shows the sectional RMSE of the resultant velocity for each model. Considering the average RMSE calculations and despite the convergence of the results, the standard k-ε model of closed channel or rigid lid model (RLM) was better than the Standard k-ε model of open channel or free surface model (FSM), while the realizable k-ε model of the open channel (FSM) was better than the realizable k-ε model of the closed channel (RLM).

Although the values of $R^2$ as shown in Table 3 for the two models of the open channel or free surface model (FSM) were similar to each other and similar to the $R^2$ values of the closed channel or rigid lid model (RLM), these values were small at the start of the curve and smaller at the end of the bend, which means that the two models were weak at this area when the direction of the flow changed from straight to curved and vice versa. In addition, this could be attributed to the complexity of flow features for these areas, which makes it not easy to be captured by numerical models. Accordingly, it could be concluded that the RLM was better at the start and end of the curve, while FSM was better at the middle of the bend. For RLM, the standard k-ε model reduced the averaged RMSE by about 42.9% and increased the averaged $R^2$ value by more than 10.5% compared to the realizable k-ε model. For FSM, the standard k-ε model reduced the averaged RMSE by about 18.3% but increased the averaged $R^2$ value by approximately 0.1% compared to the realizable k-ε model.

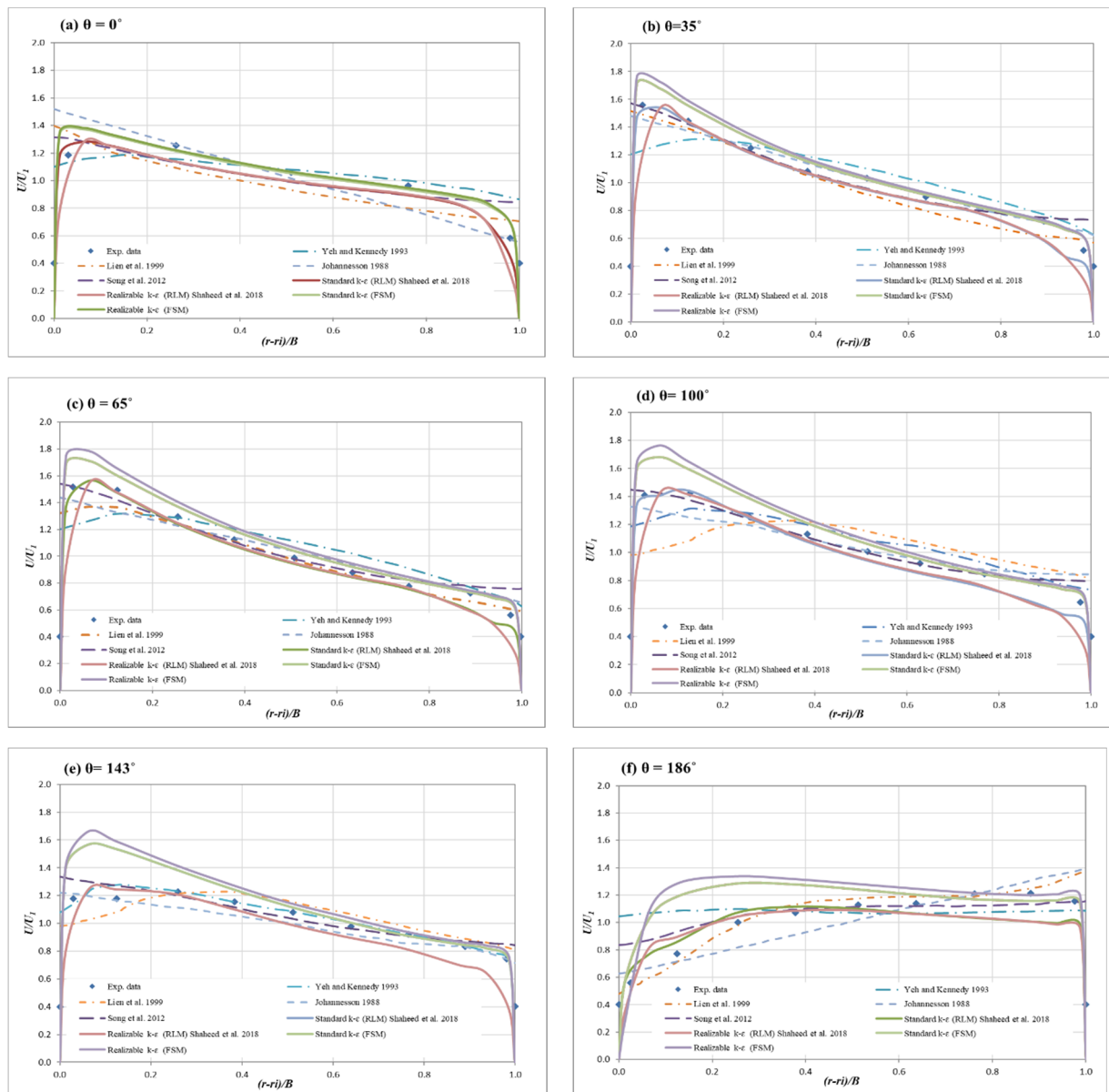**Figure 9.** The resultant velocities comparison across the dimensionless channel width: (**a**) at θ = 0°
(**b**) at θ = 35°; (**c**) at θ = 65°; (**d**) at θ = 100°; (**e**) at θ = 143°; and (**f**) at θ = 186°.

**Table 2.** RMSE estimation for resultant velocities in Figure 9.

| θ (°) | Models | | | | | | | |
|---|---|---|---|---|---|---|---|---|
| | Yeh and Kennedy | Lien et al. | Johannesson | Song et al. | Standard k-ε Model (RLM) | Realizable k-ε Model (RLM) | Standard k-ε Model (FSM) | Realizable k-ε Model (FSM) |
| 0 | 0.1515 | 0.1462 | 0.1663 | 0.1555 | 0.0972 | 0.1706 | 0.0848 | 0.0869 |
| 35 | 0.1790 | 0.1163 | 0.0782 | 0.1026 | 0.0757 | 0.1741 | 0.0718 | 0.0948 |
| 65 | 0.1771 | 0.1063 | 0.1070 | 0.0963 | 0.0733 | 0.1668 | 0.0846 | 0.1174 |
| 100 | 0.1287 | 0.1020 | 0.1339 | 0.0731 | 0.0855 | 0.1635 | 0.1063 | 0.1388 |
| 143 | 0.0476 | 0.1255 | 0.0866 | 0.0887 | 0.0975 | 0.1574 | 0.1618 | 0.1903 |
| 186 | 0.2838 | 0.0978 | 0.1682 | 0.1514 | 0.1183 | 0.1262 | 0.1917 | 0.2297 |
| Mean RMSE | 0.1613 | 0.1157 | 0.1234 | 0.1112 | 0.0912 | 0.1597 | 0.1168 | 0.1429 |

**Table 3.** $R^2$ values of resultant velocities shown in Figure 9.

| θ (°) | $R^2$ Values | | | |
|---|---|---|---|---|
| | Standard k-ε Model (RLM) | Realizable k-ε Model (RLM) | Standard k-ε Model (FSM) | Realizable k-ε Model (FSM) |
| 0 | 0.9668 | 0.9272 | 0.8939 | 0.8994 |
| 35 | 0.9895 | 0.8383 | 0.9897 | 0.99 |
| 65 | 0.9892 | 0.8575 | 0.994 | 0.9922 |
| 100 | 0.9948 | 0.8677 | 0.993 | 0.9916 |
| 143 | 0.9637 | 0.884 | 0.8859 | 0.8956 |
| 186 | 0.7494 | 0.7406 | 0.5116 | 0.5062 |

### 3.2.4. Helical Path

The helical path of the fluid particles could be represented by the vectors at the section in the middle of the bend shown in Figure 10 for the standard k-ε model and Figure 11 for the Realizable k-ε model. The vectors are more numerous and larger close to the internal bank of the curve, as the maximum velocity occurred in this area.



**Figure 10.** The velocity vectors at θ = 90° (Standard k-ε).



**Figure 11.** The velocity vectors at θ = 90° (Realizable k-ε).

### 3.3. Confluent Channel

The open channel confluence flow experiment of Shumate [23] was used to apply the model of the confluent channel. In this experiment, a branch channel joins with the main channel at a 90° angle as shown in Figure 12. The information on the channel and flow parameters is shown in Table 4.
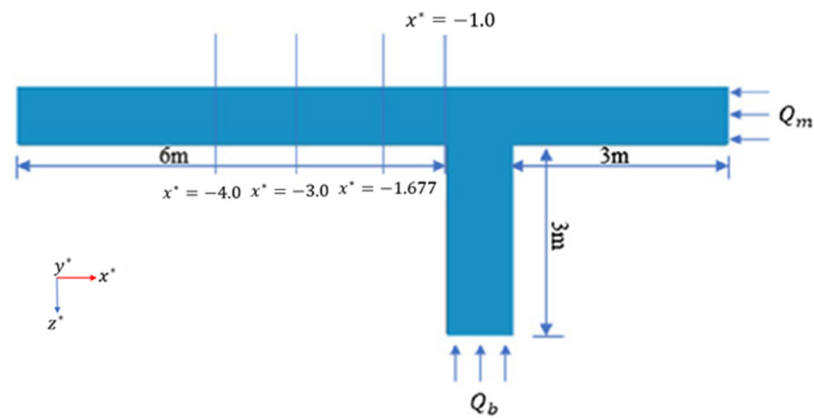
**Figure 12.** The confluent channel model (Shaheed et al., 2018) [14].

**Table 4.** The flow conditions and dimensions of the confluent channel (developed from Shumate) [23].

| Variable | Symbol | Value |
|---|---|---|
| Main channel discharge | $Q_m$ | 0.043 m$^3$/s |
| Branch channel discharge | $Q_b$ | 0.127 m$^3$/s |
| Downstream water depth | $h$ | 0.296 m |
| Channel width | $B$ | 0.914 m |
| Che'zy factor | $C$ | 60 |
| Mean velocity at downstream | $U_\infty$ | 0.628 m/s |
| Tailwater Froude number | $Fr_d$ | 0.37 |

Boundary Conditions and Mesh Generation

Figure 13 shows the confluent channel boundary conditions. They are similar to those of the curved channel mentioned previously in Section 3.1.1 because of the boundary's identical nature. The mesh is shown in Figure 14, and it was also refined for a better resolution.
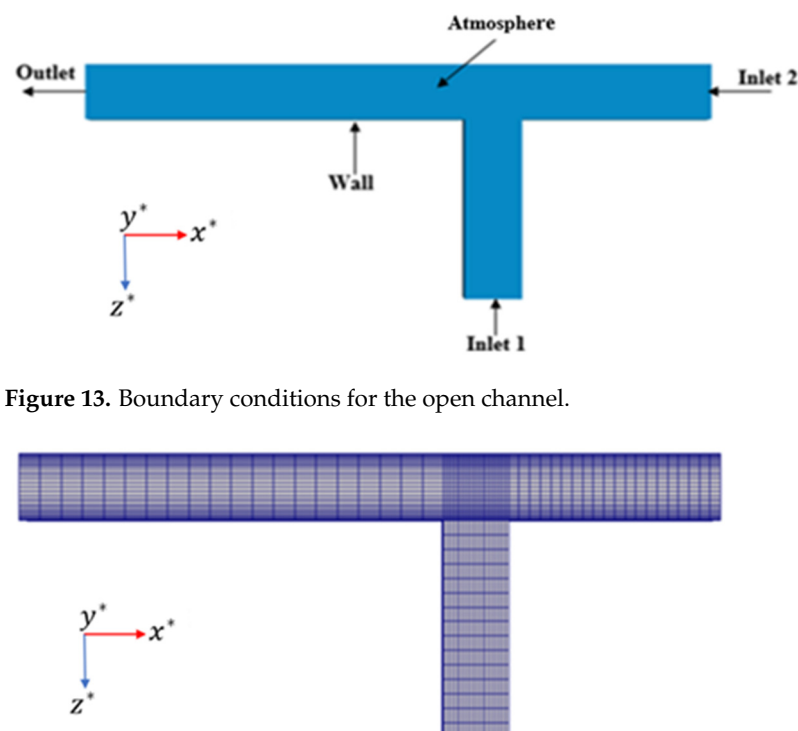


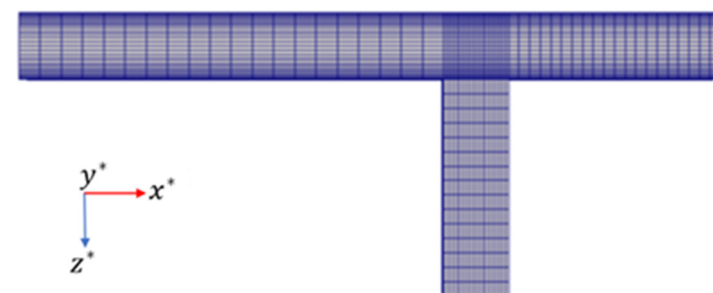**Figure 13.** Boundary conditions for the open channel.



**Figure 14.** The refined mesh.

*3.4. Results of Confluent Channel*

3.4.1. Velocity Distribution

The velocity distribution of the curved open channel is shown in Figures 15 and 16 for the two numerical models. The differences in the distribution of water surface velocity obtained by the two models were insignificant. It appeared that the maximum velocity moved towards the outside bank of the main channel.
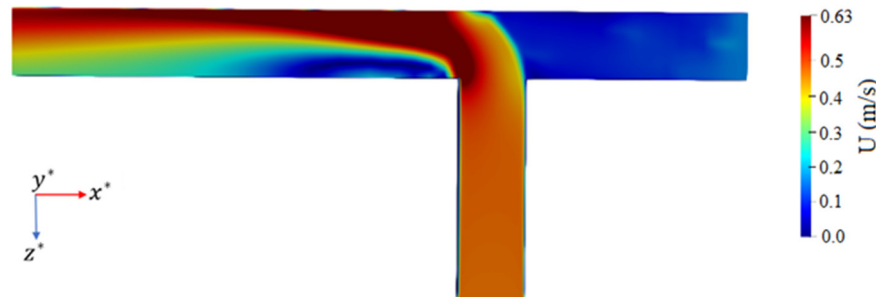


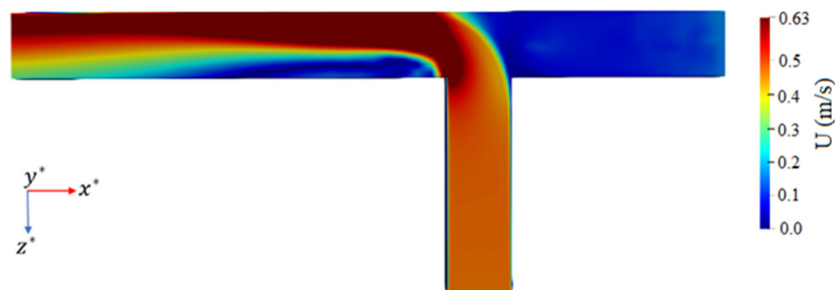**Figure 15.** The distribution of water surface velocity (Standard k-ε).



**Figure 16.** The distribution of water surface velocity (Realizable k-ε).

3.4.2. Properties of Flow Velocity

Figure 17 shows the depth-averaged velocity across the width of the channel, where: $U$ is the depth-averaged velocity magnitude, which is non-dimensionalized by $U_1$ (the downstream mean velocity); $x^* = x/B$, with the $x$ coordinate non-dimensionalized by the channel width; $z^* = z/B$, with the $z$ coordinate non-dimensionalized by the channel width; and $B$ is the channel width. The obtained results indicate that the distribution of the flow velocity for the two numerical models is somewhat similar. The higher velocity moved from the branch channel as the secondary flow entered the main channel towards the outside bank of the main channel. Some cross-sections were taken at the main channel immediately after the convergence and afterward to study the velocity curve in this area (see Figure 12). The simulated results of the numerical models were compared with the experimental data [23] and the agreement of both models was reasonable. However, for the first section, the experiment was underestimated by the two numerical models, while for the other three sections, the simulated results were close to the experimental results near the inside bank but underestimated the experimental results near the outside bank. A possible reason for the underestimation is that the non-homogeneity and anisotropy of turbulence near the outside bank were more significant, and it is typical that a RANS model cannot well predict the non-homogeneity and anisotropy of turbulence. Referring to the RMSE values of the two models shown in Table 5, the mean RMSE of the realizable k-ε model had the lowest value, which means it performed better. However, the difference between the two models was not significant.
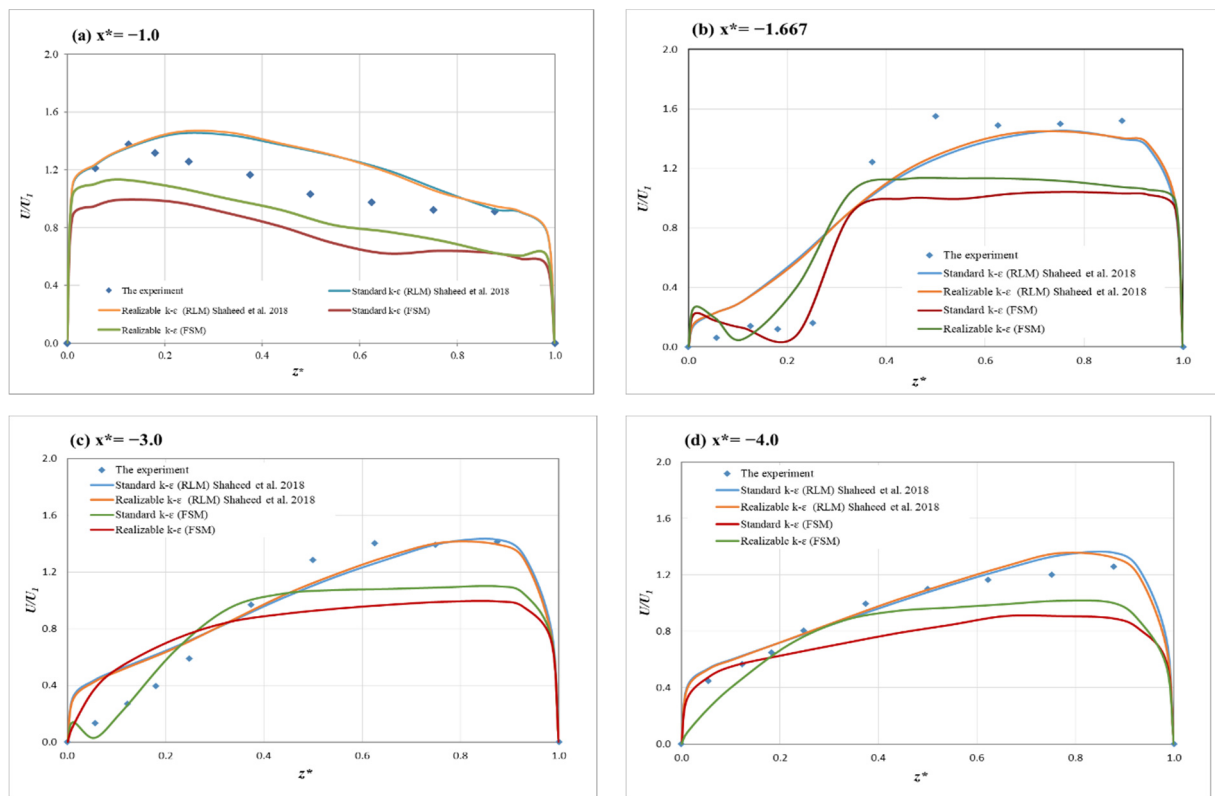
**Figure 17.** Resultant velocities across dimensionless transverse distance for confluent channel (**a**) at
x* = −1.0 (**b**) at x* = −1.667 (**c**) at x* = −3.0 (**d**) at x* = −4.0.

**Table 5.** RMSE estimation for the resultant velocities in Figure 17.

| Cross-Sections | Models | | | |
|---|---|---|---|---|
| | Standard k-ε Model (RLM) | Realizable k-ε Model (RLM) | Standard k-ε Model (FSM) | Realizable k-ε Model (FSM) |
| −1.0 | 0.1775 | 0.1798 | 0.3110 | 0.2075 |
| −1.667 | 0.2688 | 0.2610 | 0.3518 | 0.3182 |
| −3.0 | 0.1795 | 0.1700 | 0.3199 | 0.2051 |
| −4.0 | 0.0708 | 0.0687 | 0.2271 | 0.1543 |
| Mean RMSE | 0.1741 | 0.1698 | 0.3024 | 0.2212 |

The values of $R^2$ shown in Table 6 indicate that both numerical models achieved high values of $R^2$ and were close to those values of the closed channel or RLM.

**Table 6.** $R^2$ values of the resultant velocities as shown in Figure 17.

| Cross Sections | $R^2$ | | | |
|---|---|---|---|---|
| | Standard k-ε Model (RLM) | Realizable k-ε Model (RLM) | Standard k-ε Model (FSM) | Realizable k-ε Model (FSM) |
| −1.0 | 0.5872 | 0.6081 | 0.9612 | 0.9293 |
| −1.667 | 0.9231 | 0.9301 | 0.9773 | 0.9148 |
| −3.0 | 0.9583 | 0.9707 | 0.925 | 0.9176 |
| −4.0 | 0.9578 | 0.9647 | 0.9806 | 0.943 |

### 3.4.3. Helical Path

The helical path of the fluid particles can be represented by the vectors in two sections, one of them at x* = −1.667 and the other at x* = −3.0 as shown in Figures 18 and 19 for the standard k-ε model, respectively. Figures 20 and 21 represent the same sections for the realizable k-ε model, respectively.
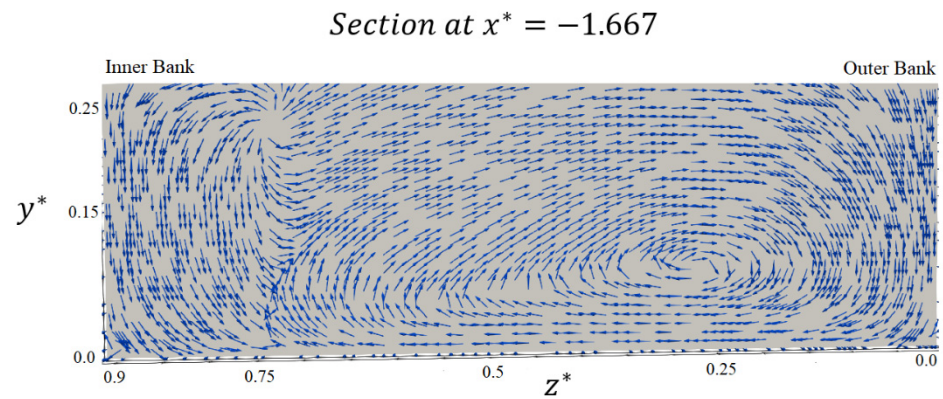


**Figure 18.** The vectors of velocity at section x* = −1.667 (Standard k-ε).
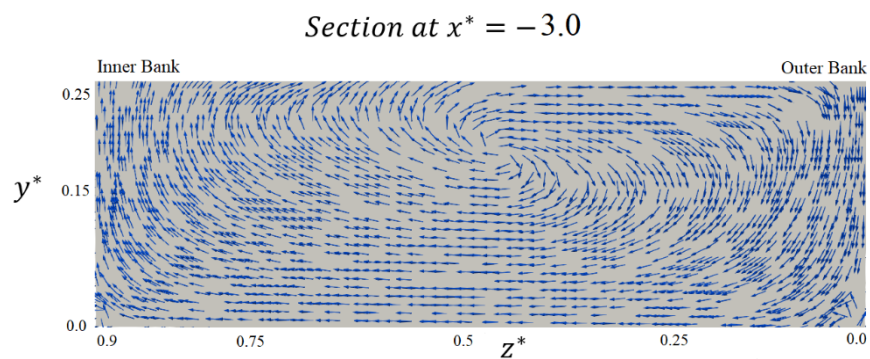


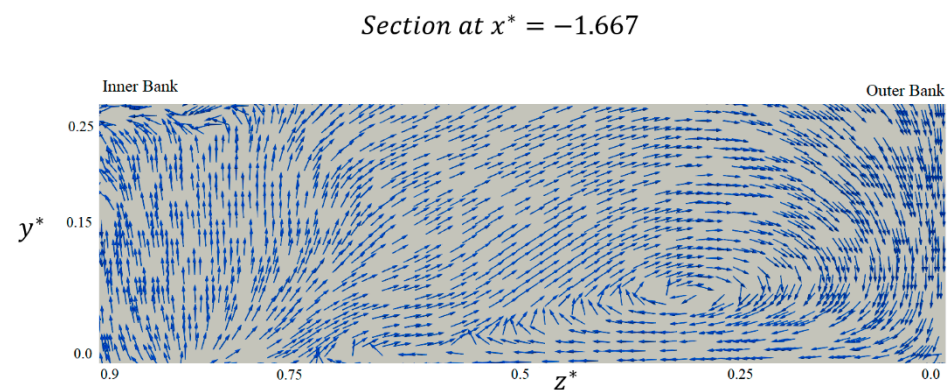**Figure 19.** The vectors of velocity at section x* = −3.0 (Standard k-ε).



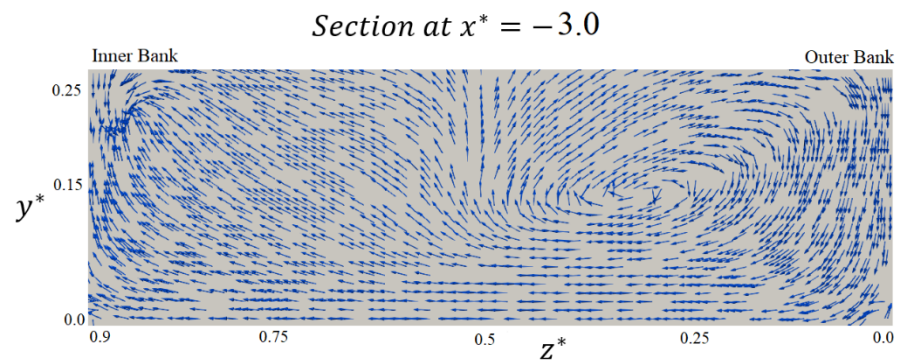**Figure 20.** The vectors of velocity at section x* = −1.667 (Realizable k-ε).

**Figure 21.** The vectors of velocity at section x* = −3.0 (Realizable k-ε).

### 3.4.4. Longitudinal Velocity Distribution

The simulated results for longitudinal velocity distribution were compared with the experimental data of Weber et al. [19] as shown in Figure 22 which represents a longitudinal section close to the water surface, and the results seem reasonable. Immediately below the channel junction and along the wall adjacent to the junction there was a zone of low velocity which represents the separation zone. Rotation within the separation region is shown as a region with positive velocity. The highest velocities occur downstream of the junction towards the outer bank of the main channel as clarified by section x* = −2.0 (Figure 23). The velocity patterns near the surface were distinctly different from the longitudinal velocity contours near the bed. Additionally, the separation zone near the surface was larger in length and width. The size of the separation zone is different as well from top to bottom due to the branch channel flow entry angle. In the area near the surface, more recirculation occurred inside the separation zone. The higher velocities immediately downstream of the junction occurred near the bed which could be attributed to the entrance angle of the lateral flow. However, the maximum velocities are readjusted to be near the surface as the contracted zone is passed [19].

### 3.4.5. Turbulent Kinetic Energy (k)

The comparison between the experimental data of Weber et al. [19] and the simulated result for turbulent kinetic energy is shown in Figure 24. It could be seen from the figure that the area of high turbulence occurred along the boundary of the passing flow and the lower part of the separation zone. It is important to note that there was no significant mixing between the branch channel flow and the main channel flow during the passing through the channel junction. However, as the mixing of the main channel's high-velocity flow and the branch channel's low-velocity flow began in the separation zone below the junction, considerable turbulence happened. The relative location of the extreme turbulent kinetic energies with respect to the separation zone was comparable for all flow situations [19].
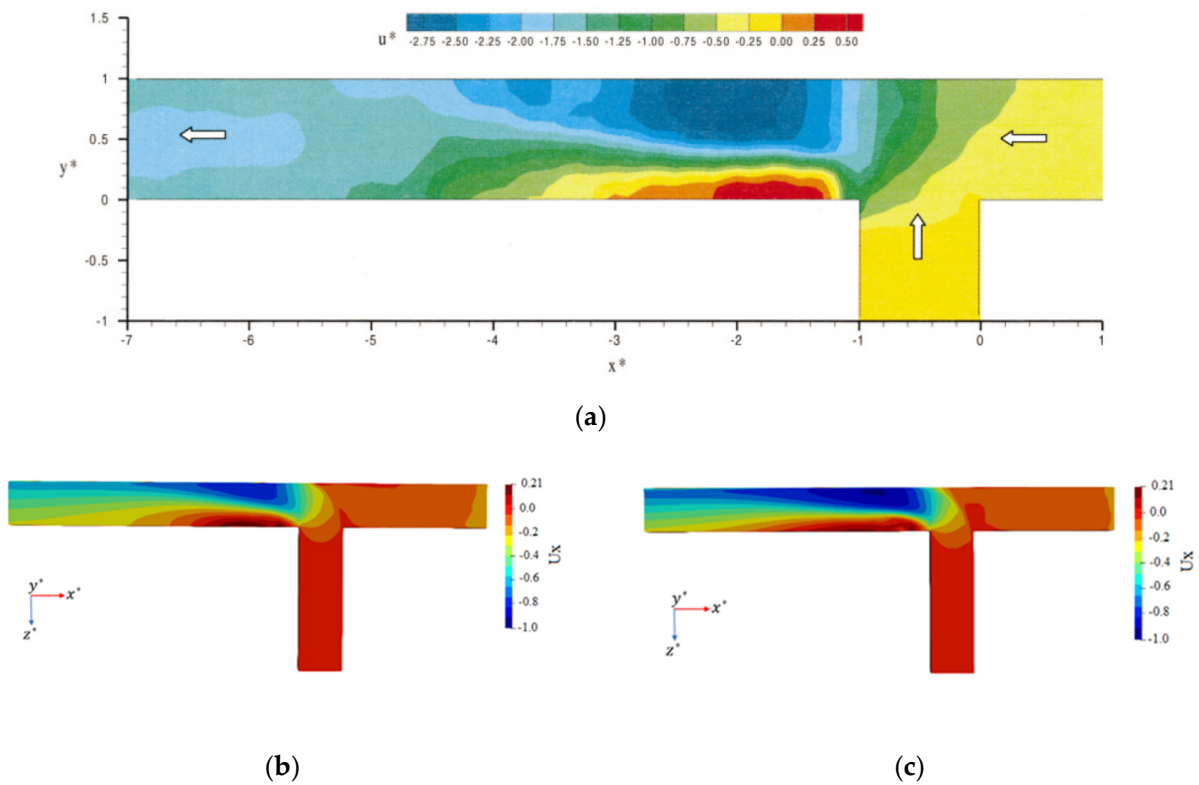
**(a)**



**(b)**                                              **(c)**

**Figure 22.** Comparison between experimental data and simulated results for longitudinal velocity. (**a**) Longitudinal velocity contour- experiment (Weber et al., 2001) [19]; (**b**) Longitudinal velocity contour for the open confluent channel (Standard k-$\varepsilon$)- Simulated; (**c**) Longitudinal velocity contour for the open confluent channel (Realizable k-$\varepsilon$)- Simulated.



**(a)**



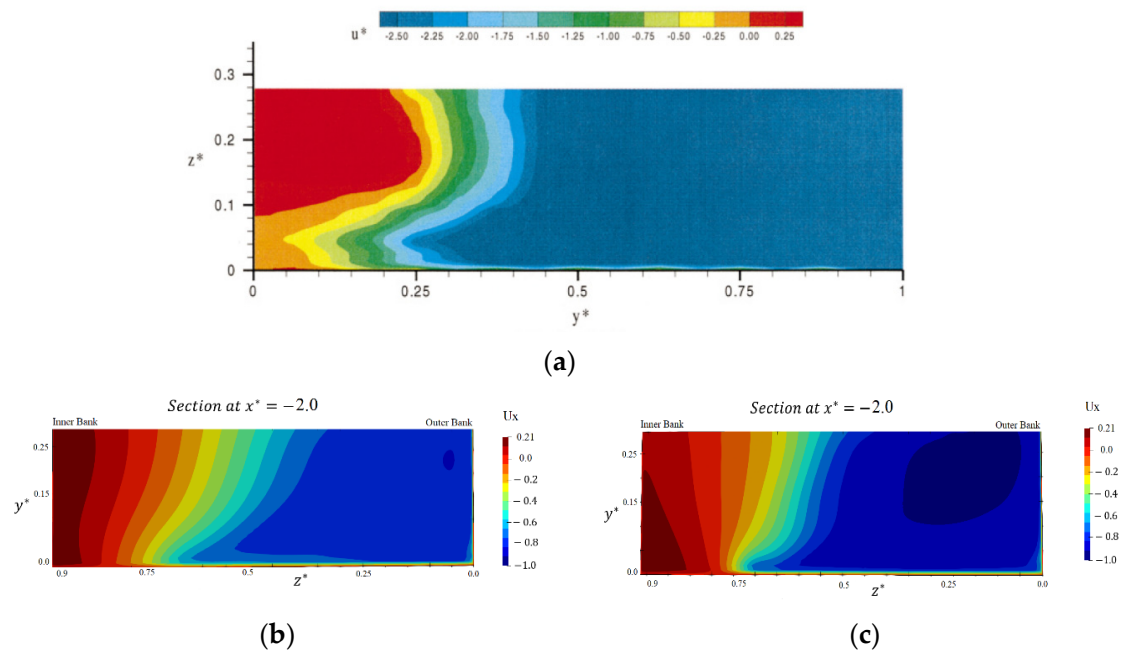**(b)**                                              **(c)**

**Figure 23.** Comparison between experimental data and simulated results for longitudinal velocity contours. (**a**) Longitudinal Velocity Contours at Cross-Section x* = −2.00 − experiment (Weber et al., 2001) [19]; (**b**) Longitudinal Velocity Contours at Cross-Section x* = −2.00 − (Standard k-$\varepsilon$)- Simulated; (**c**) Longitudinal Velocity Contours at Cross-Section x* = −2.00 − (Realizable k-$\varepsilon$)- Simulated.

(a)



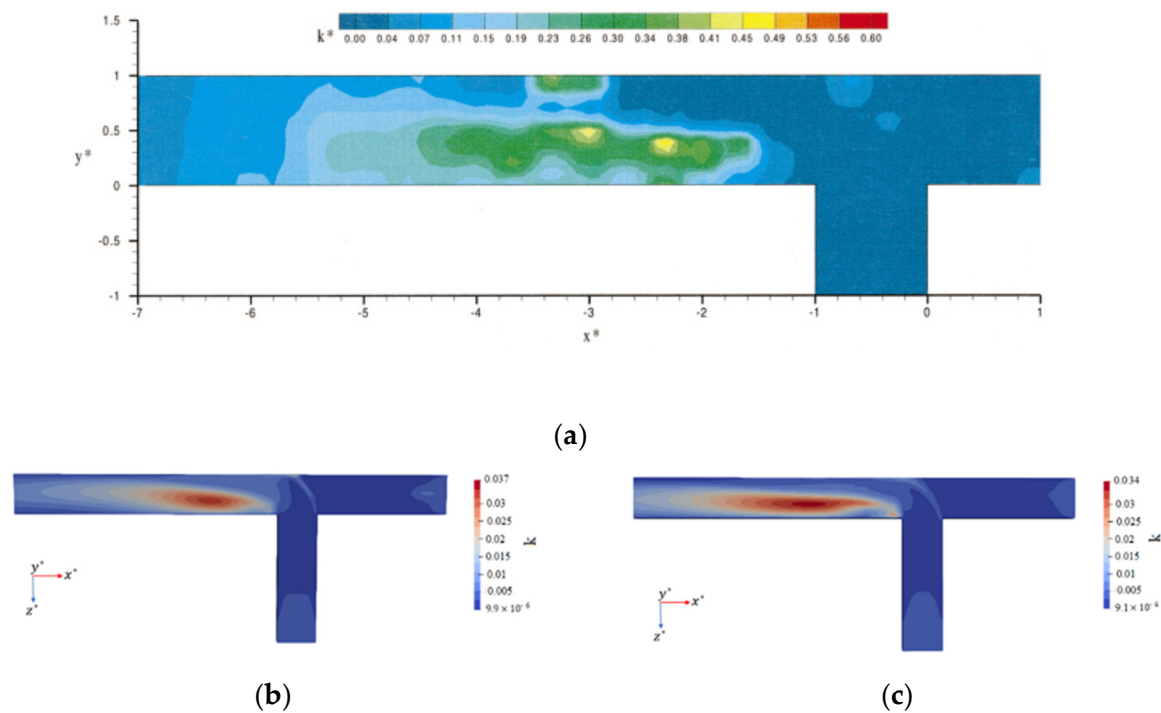(b)                                                                                     (c)

**Figure 24.** Turbulent kinetic energy distribution. (**a**) Dimensionless turbulent kinetic energy- experiment [19]; (**b**) Dimensionless turbulent kinetic energy- simulated (Standard k-ε); (**c**) Dimensionless turbulent kinetic energy- simulated (Realizable k-ε).

## 4. Discussion and Future Works

Numerical models are considered one of the important tools for predicting flow in a curved channel, allowing for various environmental studies, such as sediment transport and pollutant dispersion [37]. In this paper, the secondary flow in two types of open channels (including a 180-degree curved channel and a right-angle confluent channel) was studied using three-dimensional numerical models. The two channels were simulated using the standard k–ε and realizable k–ε turbulence models and the results were compared with the experimental data of Rozovskii [13] for the curved channel and Shumate [23] for the confluent channel. The performance of the two turbulence models was evaluated using the depth-averaged velocity across the width of the channel as shown in Figure 9 for curved channels and Figure 17 for confluent channels. In addition, RMSE and $R^2$ were also calculated for a further quantitative evaluation of the model performance. The higher velocity for the simulation of the open curved channel was close to the inner bank of the channel at the beginning of the bend and then it headed towards the outer bank near the bend exit. This was consistent with the observations obtained from the experiment. However, in most sections, the experimental data was overestimated by the two models near the inner bank, while both models performed well near the outer bank. In the last section and near the bend exit, there was a slight difference between the two numerical models and the experimental data which could be attributed to the change in the fluid direction in this area, making its characteristics very complex and difficult to capture, or it could be attributed to the weakness of these two models to capture or simulate these areas. Accordingly, it could be said that the difference between FSM and RLM was not significant, and the RLM was better at the start and end of the curve while the FSM was better at the middle of the bend. For the simulation of the open confluent channel, the higher velocity headed towards the outer bank of the main channel as the flow entered the main channel. Despite the difference between the simulated results of the two models and the experimental data seen in Figure 17 and Table 5 for RMSE, both models predicted the main characteristics of the flow reasonably well, which can be seen in the results of $R^2$ as shown in Table 6. Accordingly, it could be said that FSM is good but not as good as RLM.

A limitation of the widespread usage of 3D numerical models in practical applications was the high computational costs. However, the current simulations were conducted using a parallel computing technique on a high-performance device, and thus the computational costs were no longer a significant issue. The computational costs varied with the simulated cases, the computing device, and the status of the device. In general, it has been noticed that the computational costs of FSM were slightly higher than those of RLM simulations, and the Realizable k–ε models were more computationally expensive than the standard k–ε models.

The present study demonstrated the performance of the standard and Realizable k–ε models in predicting the flow in a channel bend and in a confluent bend and provide user experience in handling the viscosity treatments. In future studies, the validated model can be further applied to carry out additional computations to investigate how varying channel configurations affect the flow characteristics.

## 5. Conclusions

Secondary flows are one of the phenomena that occur in river curves and confluences due to the curved directions that the flow takes in such areas. The flow in these types of channels is affected significantly by the secondary flows, and its features become very complicated and are not easy to accurately capture and determine by numerical models. Unlike [14] which used a rigid lid approach, which implied no vertical displacement of the water surface, in the present study, the volume of fluid method was used to simulate the free surface displacements. This study employed two turbulence models to simulate the flow in a sharply curved channel and vertical angle confluent channel. The key conclusions of this study are concise as follows:

- For the curved channel, the two models successfully captured the general velocity distribution pattern, i.e., the higher velocity occurred near the inner bank at the start of the curve and near the outer bank at the end of the curve. In addition, both models performed reasonably well in reproducing the experimental data. For all the sections of the curve, when assessing the flow velocity, the standard k–ε model performed relatively better.
- For the confluent channel, the two models captured the main velocity characteristics correctly, i.e., the higher velocity occurred near the inner bank of the main channel as the flow entered the main channel. Moreover, both models performed reasonably well in predicting the experimental data. For all the sections taken after the junction, when assessing the flow velocity, the Realizable k–ε model performance was better.
- The current work focused on validating the numerical models and investigating the flow characteristics in some benchmark cases. In future studies, the validated model can be employed to assess the influence of different channel configurations, including the aspect ratio, the curvature, and the geometry of the confluences.

# References

1.  Vaghefi, M.; Akbari, M.; Fiouz, A.R. Experimental Investigation of the Three-dimensional Flow Velocity Components in a 180 Degree Sharp Bend. *World Appl. Program.* **2015**, *5*, 125–131.
2.  Akbari, M.; Vaghefi, M. Experimental investigation on streamlines in a 180° sharp bend. *Acta Sci. Technol.* **2017**, *39*, 425–432.
3.  Vaghefi, M.; Akbari, M.; Fiouz, A.R. An Experimental Study of Mean and Turbulent Flow in a 180 Degree Sharp Open Channel Bend: Secondary Flow and Bed Shear Stress. *KSCE J. Civ. Eng.* **2016**, *20*, 1582–1593. [CrossRef]
4.  Booij, R. Measurements and large eddy simulations of the flows in some curved flumes. *J. Turbul.* **2003**, *4*, 8–16. [CrossRef]
5.  Huang, S.; Jia, Y.; Chan, H.-C.; Wang, S.S.Y. Three-Dimensional Numerical Modeling of Secondary Flows in a Wide Curved Channel. *J. Hydrodyn.* **2009**, *21*, 758–766. [CrossRef]
6.  Constantinescu, G.; Koken, M.; Zeng, J. Simulation of flow in an open channel bend of strong curvature using Detached Eddy Simulation. In *River Flow*; Dittrich, A., Koll, K., Aberle, J., Geisenhainer, P., Eds.; Bundesanstalt Für Wasserbau: Karlsruhe, Germany, 2010; ISBN 978-3-939230-00-7.
7.  Blanckaert, K. FLow and Turbulence in Sharp Open-channel Bends. Ph.D. Thesis, Ecole Polytechnique Federale Lausanne, Lausanne, Switzerland, 2003.
8.  van Balen, W.; Blanckaert, K.; Uijttewaal, W.S.J. Analysis of the role of turbulence in curved open-channel flow at different water depths by means of experiments, LES and RANS. *J. Turbul.* **2010**, *11*, N12. [CrossRef]
9.  Abhari, M.N.; Ghodsian, M.; Vaghefi, M.; Panahpura, N. Experimental and numerical simulation of flow in a 90, bend. *Flow Meas. Instrum.* **2010**, *21*, 292–298. [CrossRef]
10. Gholami, A.; Akhtari, A.A.; Minatour, Y.; Bonakdari, H.; Javadi, A.A. Experimental And Numerical Study on Velocity Fields and Water Surface Profile in a Strongly-Curved 90° Open Channel Bend. *Eng. Appl. Comput. Fluid Mech.* **2014**, *8*, 447–461. [CrossRef]
11. Abdou, S.S.; ElMoustafa, A.M.; Samy, M. Assessing Flow Bends in Open Channels. *Int. Res. J. Adv. Eng. Sci.* **2021**, *6*, 49–54.
12. Seyedashraf, O.; Akhtari, A.A. Three-dimensional CFD Study of Free-Surface Flow in a Sharply Curved 30° Open-Channel Bend. *Eng. Sci. Technol. Rev.* **2017**, *10*, 85–89. [CrossRef]
13. Rozovskii, I. *Flow of Water in Bends of Open Channels*; [i.e., Jerusalem Israel Program for Scientific Translations; Washington, D.C., available from the Office of Technical Services, U.S. Dept. of Commerce, 1961]; Academy of Sciences of the Ukrainian SSR: Kiev, Ukraine, 1957.
14. Shaheed, R.; Mohammadian, A.; Gildeh, H.K. A comparison of standard k–ε and realizable k–ε turbulence models in curved and confluent channels. *Environ. Fluid Mech.* **2018**, *19*, 543–568. [CrossRef]
15. Best, J. Flow dynamics at river channel confluences: Implications for sediment transport and bed morphology. In *Recent Developments in Fluvial Sedimentology*; Ethridge, F.G., Flores, R.M., Harvey, M.D., Eds.; SEPM Society for Sedimentary Geology: Tulsa, OK, USA, 1987; pp. 27–35.
16. Brito, M.; Canelas, O.; Leal, J.; Cardoso, A. 3D numerical simulation of flow at a 70° open-channel confluence. In Proceedings of the V Conferência Nac. Mecânica Fluidos Termodinâmica Energ. (MEFTE), 11–12 September 2014, Porto, Portugal.
17. Song, C.G.; Seo, W.; Kim, Y.D. Analysis of secondary current effect in the modeling of shallow flow in open channels. *Adv. Water Resour.* **2012**, *41*, 29–48. [CrossRef]
18. Shakibaeinia, A.; Tabatabai, M.; Zarrati, A. Three-dimensional numerical study of flow structure in channel confluences. *Can. J. Civ. Eng.* **2010**, *37*, 772–781. [CrossRef]
19. Weber, L.; Schumate, E.; Mawer, N. Experiments on flow at a 90° open-channel junction. *J. Hydraul. Eng.* **2001**, *127*, 340–350. [CrossRef]
20. Shaheed, R.; Yan, X.; Mohammadian, A. Review and Comparison of Numerical Simulations of Secondary Flow in River Confluences. *Water* **2021**, *13*, 1917. [CrossRef]
21. Huang, J.; Weber, L.J.; Lai, Y.G. Three-Dimensional Numerical Study of Flows in Open-Channel Junctions. *J. Hydraul. Eng.* **2002**, *128*, 268–280. [CrossRef]
22. Wilcox, D.C. *Turbulence modeling for CFD*, 1st ed.; DCW Industries, Inc.: La Canada, CA, USA, 1993.
23. Shumate, E.D. *Experimental Description of Flow at an Openchannel Junction*; University of Iowa: Iowa City, IA, USA, 1998.
24. Olsen, N.R.B. *SSIIM Users' Manual*; The Norwegian University of Science and Technology: Trondheim, Norway, 2006.
25. Shumate, E.; Weber, L. Experimental Description of Combining Flows at an Open Channel Junction. *Water Resour. Eng.* **1998**, 1679–1684.
26. Yang, Q.; Liu, T.; Lu, W.; Wang, X. Numerical simulation of confluence flow in open channel with dynamic meshes techniques. *Adv. Mech. Eng.* **2013**, *5*, 860431. [CrossRef]
27. Birjukova, O.; Ludena, S.; Alegria, F.; Cardoso, A. Three dimensional flow field at confluent fixed-bed open channels. In *River Flow 2014*; Schleiss, A., De Cesare, G., Franca, M.J., Pfister, M., Eds.; Taylor & Francis Group: London, UK, 2014.
28. OpenFOAM. The Open Source CFD Toolbox Programmer's Guide, Version 3.0.1. 2015. Available online: http://foam.sourceforge.net/docs/Guides-a4/ProgrammersGuide.pdf (accessed on 8 April 2022).
29. Wendt, J. *Computational Fluid Dynamics: An Introduction*; Springer: Berlin/Heidelberg, Germany, 2008.
30. Launder, B.E.; Spalding, D.B. *Mathematical Models of Turbulence*; Academic Press: Cambridge, MA, USA, 1972.
31. Shih, T.; Zhu, J.; Lumley, J. A new Reynolds stress algebraic equation model. *Comput. Methods Appl. Mech. Eng.* **1995**, *125*, 287–302. [CrossRef]

32. Launder, B.E.; Spalding, D.B. The numerical computation of turbulent flows. *Comput. Methods Appl. Mech. Eng.* **1974**, *3*, 269–289. [CrossRef]
33. Yan, X.; Rennie, C.D.; Mohammadian, A. A three-dimensional numerical study of flow characteristics in strongly curved channel bends with different side slopes. *Environ. Fluid Mech.* **2020**, *20*, 1491–1510. [CrossRef]
34. Lien, H.C.; Hsieh, T.Y.; Yang, J.C.; Yeh, K.C. Bend-flow simulation using 2D depth-averaged model. *J. Hydraul. Eng.* **1999**, *125*, 1097–1108. [CrossRef]
35. Yeh, K.C.; Kennedy, J.F. Moment model of nonuniform channel-bend flow. I: Fixed beds. *J. Hydraul. Eng.* **1993**, *119*, 776–795. [CrossRef]
36. Johannesson, H. Theory of River Meanders. Ph.D. Thesis, University of Minnesota, Minnesota, MN, USA, 1988.
37. Shaheed, R.; Mohammadian, A.; Yan, X. A Review of Numerical Simulations of Secondary Flows in River Bends. *Water* **2021**, *13*, 884. [CrossRef]